




Article

Noninvasive Measurement of [¹¹C]PiB Distribution Volume Using Integrated PET/MRI

Hidehiko Okazawa ^{1,*}, Masamichi Ikawa ^{1,2}, Tetsuya Tsujikawa ¹, Akira Makino ¹,
Tetsuya Mori ¹, Yasushi Kiyono ¹ and Hirotaka Kosaka ³

¹ Biomedical Imaging Research Center, University of Fukui, Eiheiji-cho 910-1193, Japan; iqw@u-fukui.ac.jp (M.I.); awaji@u-fukui.ac.jp (T.T.); amakino@u-fukui.ac.jp (A.M.); morit@u-fukui.ac.jp (T.M.); ykiyono@u-fukui.ac.jp (Y.K.)

² Department of Advanced Medicine for Community Healthcare, Faculty of Medical Sciences, University of Fukui, Fukui 910-1193, Japan

³ Department of Neuropsychiatry, Faculty of Medical Sciences, University of Fukui, Fukui 910-1193, Japan; hirotaka@u-fukui.ac.jp

* Correspondence: okazawa@u-fukui.ac.jp; Tel.: +81-776-61-8491

Received: 4 November 2020; Accepted: 22 November 2020; Published: 24 November 2020



Abstract: A noninvasive image-derived input function (IDIF) method using PET/MRI was applied to quantitative measurements of [¹¹C] Pittsburgh compound-B (PiB) distribution volume (DV) and compared with other metrics. Fifty-three patients suspected of early dementia (71 ± 11 y) underwent 70 min [¹¹C]PiB PET/MRI. Nineteen of them (68 ± 11 y) without head motion during the scan were enrolled in this study and compared with 16 age-matched healthy controls (CTL: 68 ± 11 y). The dynamic frames reconstructed from listmode PET data were used for DV calculation. IDIF with metabolite correction was applied to the Logan plot method, and DV was normalized into DV ratio (DVR) images using the cerebellar reference (DVR_L). DVR and standardized uptake value ratio (SUVR) images were also calculated using the reference tissue graphical method (DVR_r) and the 50–70 min static data with cerebellar reference, respectively. Cortical values were compared using the 3D-T1WI MRI segmentation. All patients were assigned to the early Alzheimer’s disease (eAD) group because of positive [¹¹C]PiB accumulation. The correlations of regional values were better for DVR_L vs. DVR_r ($r^2 = 0.97$) than for SUVR vs. DVR_r ($r^2 = 0.88$). However, all metrics clearly differentiated eAD from CTL with appropriate thresholds. Noninvasive quantitative [¹¹C]PiB PET/MRI measurement provided equivalent DVRs with the two methods. SUVR images showed acceptable results despite inferior variability and image quality to DVR images.

Keywords: PET/MRI; amyloid imaging; distribution volume; SUVR; quantitative analysis; IDIF

1. Introduction

Molecular imaging methods are used for the clinical diagnosis of neurodegenerative diseases based on visual delineation of functional or pathological changes in the brain. Recently, the amyloid and tau imaging technique using positron emission tomography (PET) has become widely used for the differential diagnosis of dementia and is considered to be important particularly for diagnosis of Alzheimer’s disease (AD) [1]. The accumulation reflects pathologic changes of aggregation of amyloid and neurofibrillary tangles caused by phosphorylated tau. Many simplified methods for evaluation of the accumulation intensity have also been developed. Several studies attempted to simplify quantitative PET measurements with [methyl-¹¹C]-2-(4'-methyl-aminophenyl)-6-hydroxybenzothiazole ([¹¹C]PiB) using the reference tissue graphical analysis method and the image-derived input function (IDIF) method [2–5], where accuracies were compared with quantitative measurements of distribution

volume (DV) with arterial blood samples to estimate the true input function. In comparisons of these quantitative metrics and standardized uptake values (SUV) obtained from static images in the later phase, SUV ratio (SUVR) values normalized by cerebellar cortical counts, which is now usually used for the evaluation of cerebral tracer accumulation, correlated well with the DV ratio (DVR) in quantitative analysis [2–5].

The accuracy of the IDIF method for quantitative evaluation of various metrics in PET studies is controversial, and many correction methods such as partial volume (PVC) and spillover, and arterial or arterialized venous blood correction have been applied for [¹¹C]PiB PET [2,5]. If the arterial input function (AIF) requires metabolite correction to estimate the real plasma input, the metabolite fraction or unchanged fraction of the tracer should be determined and applied to the whole blood IDIF. Mourik et al. (2009) compared three different brain PET tracers and concluded that [¹¹C]PiB PET might require blood count calibration to adjust the radioactivity concentration to a real AIF. However, AIFs obtained from blood samples may be unreliable due to substantial errors caused by sticking of the tracer [5]. In such cases of highly lipophilic ligands, image-derived estimation of arterial radioactivity with appropriate correction methods including metabolite ratio may be more reliable than measurement with sampling blood in clinical studies.

We established a new calibration method using an integrated PET/MRI scanner to estimate precise arterial radioactivity from noninvasive IDIF [6]. In the present study, we applied our new IDIF method for estimation of the true input function without blood sampling, and compared regional values with DVR from graphical reference tissue method (DVR_r) and SUVR. A high quality of IDIF estimation is an advantage of PET/MRI because of simultaneous acquisition of PET and MRI images in the same location and high reliability of IDIF counts by improvement of PET detectors [6,7]. To correct the metabolite fraction in the arterial blood, a Hill-type function was applied to the IDIF curves [5,8], eliminating the need for invasive arterial blood sampling in the deep PET/MRI gantry. We employed the segmentation method using individual anatomical images from MRI to differentiate the gray and white matters as well as cerebrospinal fluid (CSF) spaces. In this way, we could obtain precise regional values by reducing individual variability. The co-registration step of PET and MRI was eliminated by the simultaneous image acquisition. Using these new techniques, the thresholds of DVR and SUVR for diagnosis were determined and the diagnostic accuracies of these metrics were compared. DVR and other quantitative values have been compared between calculation methods of arterial input with metabolite correction and reference tissue method, and showed linear correlations [2–5,9]. SUVR is now widely used as a simple and easily obtained metric from a single static scan for 10–20 min in the later phase, while it has greater variation and substantial overlap between positive (AD) and negative (non-AD) patients [9,10]. We compared these metrics to evaluate feasibility of the new IDIF method using integrated PET/MRI.

2. Materials and Methods

2.1. Subjects

Fifty-three patients with decline of cognitive function (26 males and 27 females, 71 ± 11 y) who were diagnosed as mild cognitive impairment (MCI) or early Alzheimer's-type dementia (DAT) were enrolled in a [¹¹C]PiB PET/MRI study to evaluate cerebral amyloid deposition for assessment of pathophysiologic changes in dementia. A 70 min dynamic PET/MRI scan was performed for all patients; however, 19 patients showed negative [¹¹C]PiB accumulation and 15 patients could not keep the same head position for the whole scan time. Finally, 19 patients (9 males and 10 females, 68 ± 11 y) who completed the 70 min scan without head motion were included in the quantitative evaluation of amyloid deposition. We recruited 16 age-matched healthy volunteers (10 males and 6 females, 68 ± 11 y) as a control group (CTL). All participants were interviewed to evaluate their cognitive ability using the Mini Mental State Examination (MMSE), and their cognitive ability has not declined for more than two years since the study. The study was approved by the Ethics Committee of the University

of Fukui, Faculty of Medical Sciences (study protocol # 20170225, 25 February 2017), based on its guidelines (Ethical Guidelines for Medical Science Research with Humans) as well as the Helsinki Declaration of 1975 (revised in 1983). Written informed consent was obtained from each patient.

2.2. PET/MRI Scanner

A whole-body PET/MRI scanner (Signa PET/MR, ver. 26, GE Healthcare, Milwaukee, WI, USA) was used for simultaneous PET and MRI data acquisition [6,11]. The scanner permits PET acquisition of 89 image slices in 3D mode, with a slice thickness of 2.76 mm. Performance tests showed the intrinsic resolution of PET images to be 4.2–4.3 mm full width at half maximum (FWHM) in the transaxial direction. The PET/MRI scanner was calibrated beforehand with a dose-calibrator (CRC-12, Capintec Inc., NJ, USA) using a pool phantom and ^{18}F -solution, according to the scanner manufacturer's guidelines [6,7].

2.3. PET and MRI Image Acquisition and PET Reconstruction

The patients underwent brain PET/MRI scans using a standard head coil (8-channel HD Brain, GE Healthcare) for simultaneous PET and MRI acquisition [6,7]. A 70 min list-mode 3D PET scan in time-of-flight (TOF) acquisition was started at the time of a bolus tracer injection of 700–750 MBq [^{11}C]PiB via the antecubital vein. During the PET scan, a 3D radial MR acquisition for the zero-echo time (ZTE) method in the axial direction was performed for attenuation correction (AC) of PET data with the following parameters: field of view (FOV) 264 mm, matrix $110 \times 110 \times 116$, voxel size $2.4 \times 2.4 \times 2.4 \text{ mm}^3$, flip angle 0.8° , number of excitations 4, bandwidth $\pm 62.5 \text{ kHz}$, and acquisition time of 41 s [12,13]. In the ZTE-AC method, the following process was used to create the MR-AC map based on a previous study [12]. Briefly, pre-filtering and histogram-based normalization were followed by intensity-based segmentation of the head, bias correction, identification of voxels affected by partial volume effects, and segmentation of the sinus, bone, and cavity masks. A pseudo-CT map was then generated with bone tissue scaled linearly based on the ZTE intensity. This mapping was determined by fitting of registered CT and ZTE data in the bone density range. To convert the pseudo-CT into a MR-AC map, the images were re-sampled with a $60 \times 60 \times 25 \text{ cm}^3$ field of view (FOV) in a $128 \times 128 \times 89$ matrix, and finally re-scaled to 511 keV attenuation coefficients.

Dynamic PET images were reconstructed from the PET data using the 3D ordered subset expectation maximization (OSEM) method and point spread function modeling algorithm in 39 frames of $12 \times 5 \text{ s}$, $6 \times 10 \text{ s}$, $3 \times 20 \text{ s}$, $4 \times 30 \text{ s}$, $5 \times 60 \text{ s}$, $4 \times 5 \text{ min}$, and $4 \times 10 \text{ min}$. The following OSEM parameter set was applied for PET image reconstruction: subset, 28; iteration, 3; transaxial post-gaussian filter cutoff, 3 mm in 256 mm FOV, and $2 \times 2 \text{ mm}^2$ pixel size. Decay of radioactivity in the dynamic PET data was corrected to the starting point of each scan [14].

3D TOF MR angiography (MRA) and other anatomical MR images such as T2-weighted (T2WI) and FLAIR were acquired in the same position during the PET scan. High-resolution 3D-T1-weighted (T1WI) anatomical MRI was also collected using the following parameters: repetition time = 8.5 ms; echo time = 3.2 ms; flip angle = 12° ; FOV = 256 mm; 256×256 matrix; 136 slices; voxel dimension = $1.0 \times 1.0 \times 1.0 \text{ mm}^3$ [6,14].

2.4. Distribution Volume and SUV Image Calculation

Arterial time–activity curves (TACs) were obtained from the dynamic [^{11}C]PiB-PET data using the IDIF method described previously [14]. Details of the IDIF estimation from PET/MRI data and its calibration method are described elsewhere [6,7]. In brief, the average image of the initial phase (10–40 s) of dynamic PET data was used to extract voxels only inside the internal carotid artery (ICA), where the 30 most intensely radioactive voxels were selected as the volume of interest (VOI) mask at the region of the clinoid to ophthalmic segment of the internal carotid artery (ICA) [15]. Individual 3D TOF-MRA images were used to verify the location of the arterial VOI mask precisely on the ICA. Arterial TACs in total blood radioactivity concentration were obtained by applying the ICA VOI masks

to the 70 min dynamic PET data [7]. Before estimating arterial TACs using the IDIF method, PET counts in two phases were determined appropriately, that is, the maximal count or average count for each slice in the VOI mask. In the first phase, average values of maximal counts obtained from 3 to 5 slices in the VOI mask for each frame were used in the initial 40–50 s. In the second phase, the maximal values of each slice mean in the VOI mask were also calculated for each frame up to 70 min, and these two phases were combined [6]. In order to estimate the true plasma input function with metabolite correction (C_p) from the IDIF TAC, the unmetabolized fraction (R) was estimated using a Hill-type function as follows [5,8]:

$$R(t) = \alpha \cdot t^\beta / (t^\beta + \gamma),$$

where t (min) is the time after the tracer injection and α , β , γ are constants determined by a nonlinear least squares fitting. To estimate optimal constants, the unchanged plasma [^{11}C]PiB fractions reported in a couple of previous studies were applied [2,4].

DV images (mL/g) were calculated on a pixel-by-pixel basis from linear regression slopes of the Logan plot method using C_p [16,17]. The last 50–70 min data plots were used for DV slope calculation. The DV images were then converted to DVR images using the mean DV value of the cerebellar cortex as a reference [9]. The Logan's reference tissue graphical method was also applied to DVR_r image calculation using a TAC of the cerebellar cortex as a reference [9,17,18].

SUV images were calculated from static images of the 50–70 min time frame of the list-mode PET data, that is, the average accumulation during this period. Each static image was corrected for the individual patient's body weight (BW: kg) and injection dose (ID: MBq) as follows: $\text{SUV} = (\text{PET count concentration [kBq/mL]}) / (\text{ID/BW})$ [14]. To compare [^{11}C]PiB accumulation in the brain, each SUV image was normalized by the individual SUV mean of the cerebellar cortex and saved as the SUV ratio (SUVR) image [10].

2.5. Statistical Analyses

We used PMOD software (version 3.9; PMOD Technologies Ltd., Zurich, Switzerland) to compare the regional DVR and SUVR values between the early AD (eAD) and CTL groups. Image parcellation was performed in PMOD, and the brain regions were segmented into 78 brain regions using the individual 3D-T1WI MRI image data. Regional values of SUVR and DVRs of Logan plot (DVR_L) and reference tissue graphical methods (DVR_r) were classified into each lobe, basal ganglia, and cerebellum from the individual regions of interest (ROIs) determined by the 3D-T1WI segmentation. The locations of PET and MRI were exactly the same due to simultaneous image acquisition in the PET/MRI scanner without subject head motion during the scan. The head position was confirmed by two anatomical MRI images at the beginning and end of PET acquisition. Repeated measures analysis of variance (ANOVA) with a post hoc paired t -test was applied to analyze differences in the values of regional DVRs and SUVR between eAD and CTL. Correlations of regional DVRs and SUVR values were also evaluated for linearity by Pearson's regression analysis. $p < 0.05$ was considered significant. To determine the optimal cutoff value for differentiating two groups of CTL and AD, receiver operating characteristic (ROC) curve analysis was applied to the three metrics.

A general linear model in Statistical Parametric Mapping (SPM12; <http://www.fil.ion.ucl.ac.uk/spm/>, Wellcome Trust Centre for Neuroimaging, London, UK) was used to evaluate differences between images of DVR_r , DVR_L , and SUVR for the eAD and CTL groups. The PET images were anatomically normalized to the Montreal Neurological Institute (MNI) space with a voxel size of $2 \times 2 \times 2 \text{ mm}^3$ using individual 3D-T1WI images and the template provided by SPM12. After the normalized images were spatially smoothed with a 10 mm Gaussian filter for group comparisons, each image pertaining to z values was entered into SPM12 with two-sample t -tests. We applied statistical thresholds of voxel-wise $p < 0.001$ uncorrected and cluster-level $p < 0.05$ family-wise error (FWE) corrected, for multiple comparisons in the whole brain.

3. Results

All patients showed positive cortical [^{11}C]PiB accumulation and were assigned to the eAD group, while volunteers in the CTL group showed negative accumulation. There were no differences in age range, mean age, and gender ratio between the two groups. The MMSE scores for cognitive status were significantly different between the eAD (23.6 ± 3.3) and CTL (28.6 ± 2.6) groups ($p < 0.00001$).

Figure 1 shows representative TACs of the arterial IDIF (solid line) and plasma input C_p corrected for the metabolite fraction (dashed line). The optimal parameters of the Hill-type function for C_p estimation were determined as $\alpha = 1.62$, $\beta = -0.92$, and $\gamma = 0.47$ by a nonlinear least squares fitting. The insert graph of Figure 1 shows changes in the unmetabolized fraction as a function of time after the tracer injection. The TACs were almost the same for the IDIF and C_p in the initial frames, and gradually separated after the capillary phase.

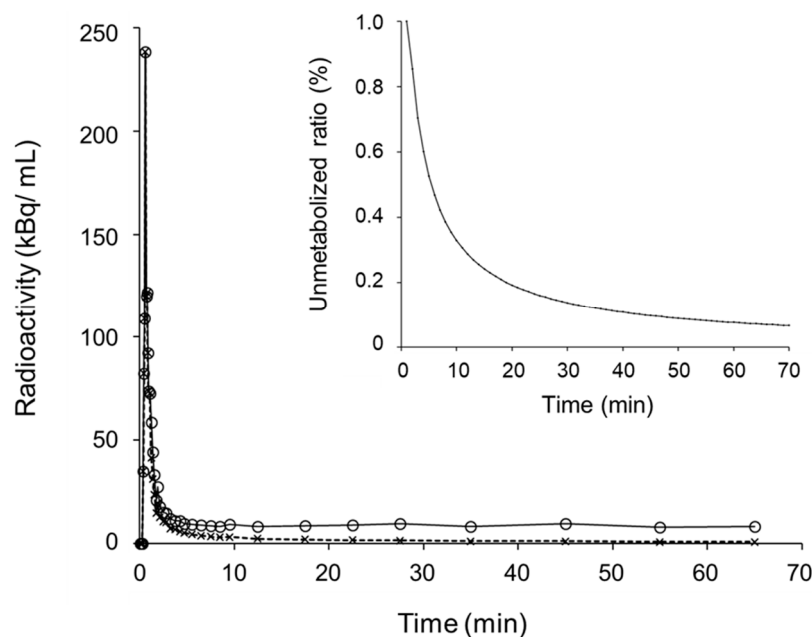


Figure 1. Representative time–activity curves (TAC) of the arterial blood (○) obtained from the image-derived input function (IDIF) method and metabolite-corrected plasma input (×) in a healthy control. Insert shows an arterial unmetabolized [^{11}C]PiB ratio curve defined by a Hill-type function.

Representative TACs of the cerebral (solid line) and cerebellar (dashed line) cortices from each group are given in Figure 2. Logan plots for [^{11}C]PiB PET showed good linear regressions in the later phases (black solid and dashed lines) in both eAD and CTL patients. The slopes of the regression lines were significantly different between the cerebral and cerebellar cortices in eAD patients (Figure 2d), while they were very close in controls (Figure 2b). The reference tissue graphical method based on the Logan plot method showed good linear correlations in the later phase (gray lines in Figure 2b,d); however, the slopes were completely different from the Logan plots because the slopes represent DV and DVR, respectively.

Figure 3 shows representative images calculated from the [^{11}C]PiB PET data of CTL and eAD subjects. DVR_L images showed better contrast for both subjects compared with DVR_r and SUVR. This tendency was observed in all subjects studied. Regional cortical values obtained from the anatomical segmentation of the brain are given in Table 1. All regional values were significantly greater in eAD subjects than in CTL. The values of the posterior cingulate cortex (PCC) were greater than other cortical regions, while the DVRs in the parietal lobe were not significantly different from those in the PCC.

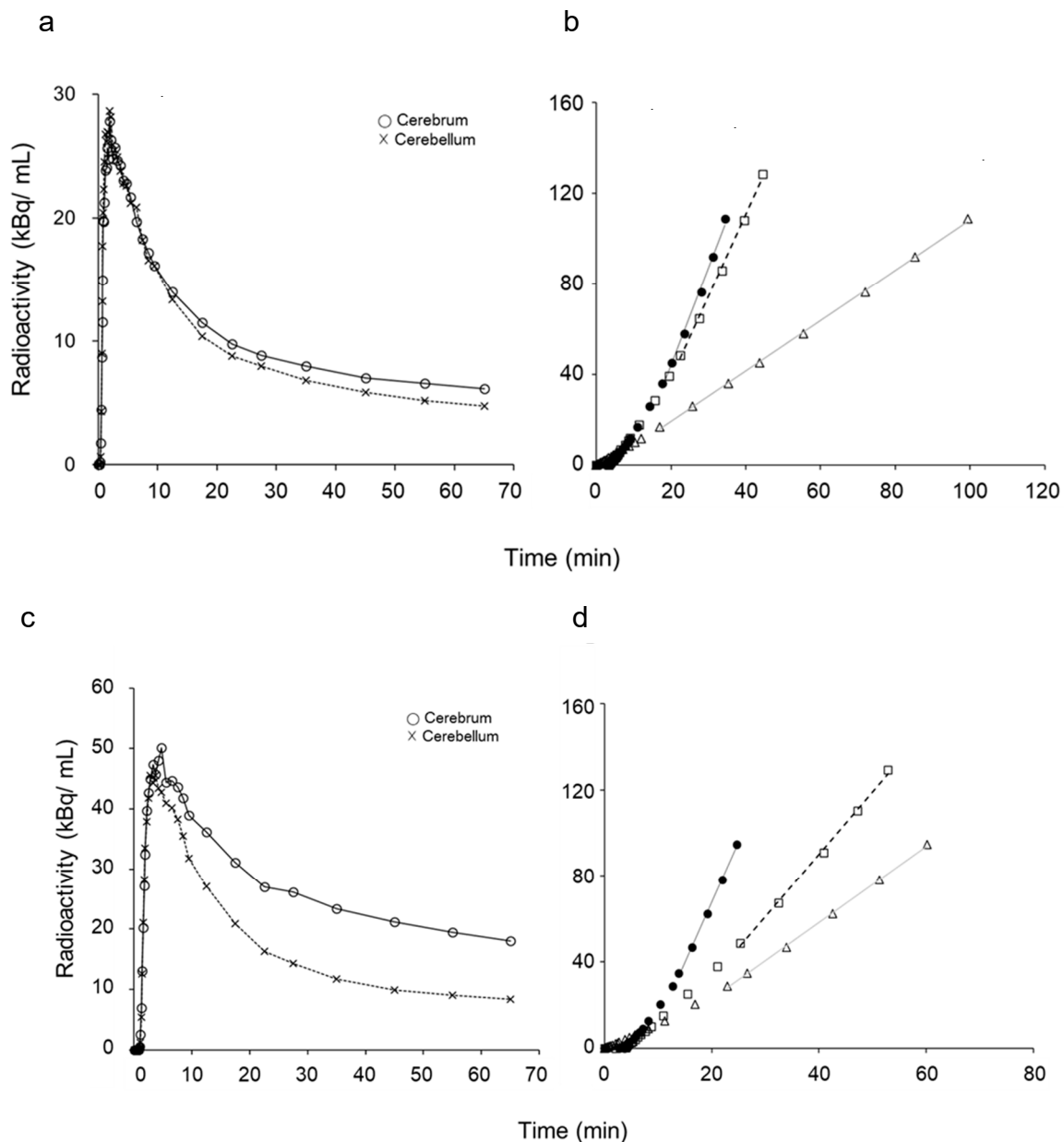


Figure 2. Representative cortical TACs of cerebrum (○) and cerebellum (×) obtained from dynamic PET data for each group of healthy control (CTL) (a) and early Alzheimer's disease (eAD) subjects (c). Logan plots of [¹¹C]PiB PET show good linear correlations in the later phases of a control (b) and an AD patient (d). The slopes of the regression lines were significantly different between cerebral cortex (● and solid line) and cerebellum (□ and dashed line) in AD patients (d), while they were similar in controls (b). The reference tissue graphical plot method also showed good linear correlations in the later phase (△ and gray line), but the slopes were completely different from the Logan plots because the cerebellar TACs were used for distribution volume ratio (DVR) calculation.

Regional values from all subjects were plotted to observe correlations between DVR_r vs. DVR_L and DVR_r vs. SUVR (Figure 4). DVR_r and DVR_L showed a better correlation ($r^2 = 0.97$) than that of DVR_r and SUVR ($r^2 = 0.88$). The variance in correlation was greater for DVR_r vs. SUVR than for DVR_r vs. DVR_L . However, SPM analysis did not show regional differences among the images of DVR_r , DVR_L , and SUVR in each group of CTL and eAD subjects. The Bland–Altman plots after correction with equations of linear regression for DVR_r vs. DVR_L (Figure 5a) and DVR_r vs. SUVR (Figure 5b) show significantly greater variance for the latter plot ($p < 0.0001$) than for the former. Figure 5c shows

the Balnd–Altman plot for correlation between DVR_L vs. $SUVR$, which also shows a greater variance compared with DVR_r vs. DVR_L (Figure 5a).

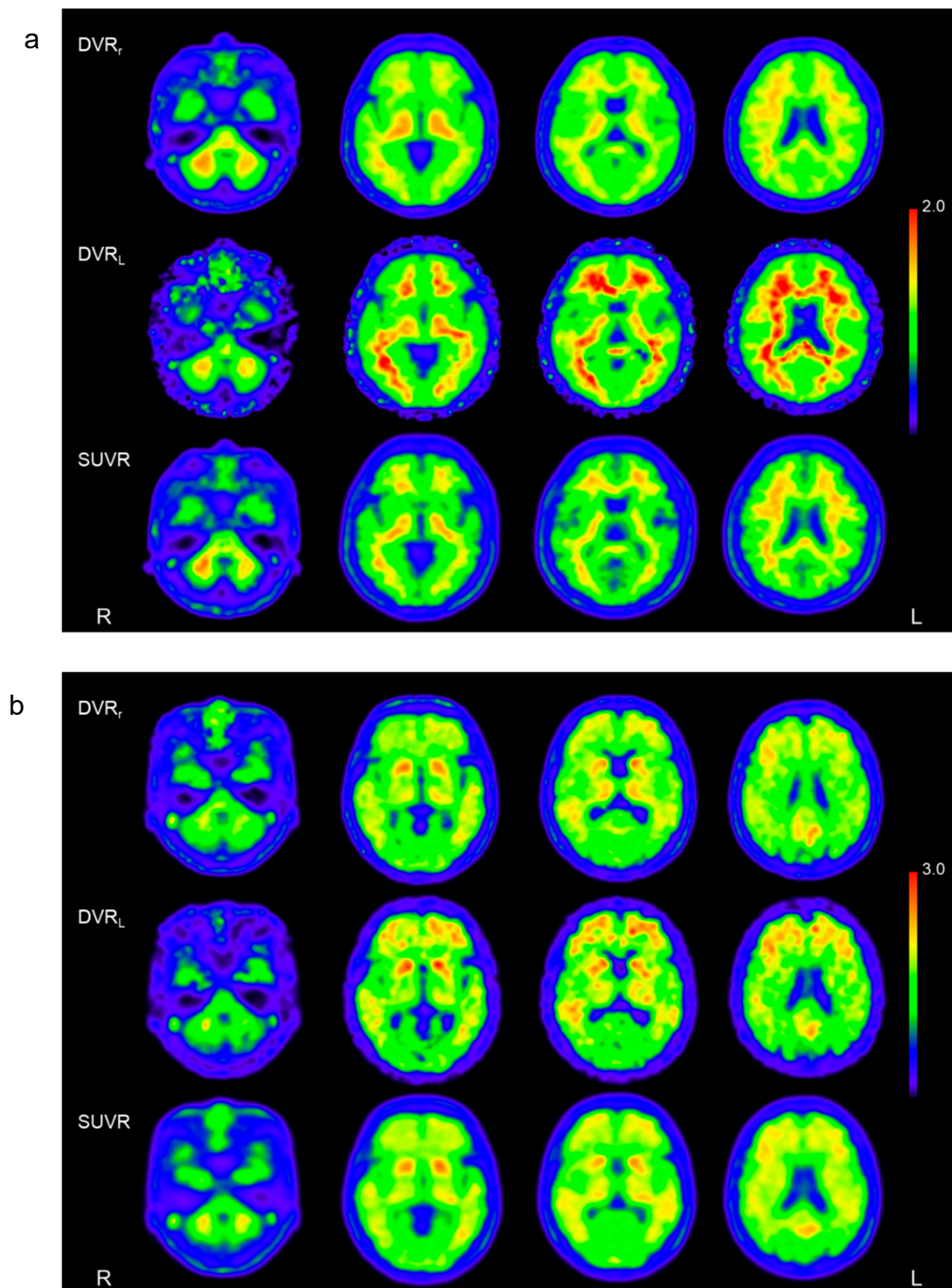


Figure 3. Representative images calculated from the $[^{11}\text{C}]\text{PiB}$ PET data of CTL (a) and eAD subjects (b). Images of distribution volume ratio calculated using the Logan plot method (DVR_L) and metabolite-corrected IDIF (middle row) showed better contrast for both groups compared with distribution volume ratio from the reference tissue graphical method (DVR_r) and standardized uptake value ratio ($SUVR$) (upper and bottom row, respectively).

Table 1. Regional DVR (mL/min/100 g) and SUVR values (mean ± SD).

		DVR _r		DVR _L		SUVR	
		CTL	eAD	CTL	eAD	CTL	eAD
Frontal	L	1.10 ± 0.11	1.78 ± 0.23 ^{†,*}	1.22 ± 0.14	2.14 ± 0.32 ^{†,*}	1.20 ± 0.13	2.00 ± 0.30 ^{†,*}
	R	1.13 ± 0.10	1.79 ± 0.25 ^{†,*}	1.24 ± 0.13	2.17 ± 0.38 [†]	1.23 ± 0.13	2.04 ± 0.32 ^{†,*}
Temporal	L	1.07 ± 0.05	1.52 ± 0.16 ^{†,*}	1.13 ± 0.06	1.72 ± 0.22 ^{†,*}	1.17 ± 0.08	1.78 ± 0.27 ^{†,*}
	R	1.07 ± 0.05	1.53 ± 0.16 ^{†,*}	1.13 ± 0.06	1.74 ± 0.23 ^{†,*}	1.16 ± 0.08	1.79 ± 0.28 ^{†,*}
Parietal	L	1.11 ± 0.11	1.87 ± 0.22 ^{†,*}	1.18 ± 0.12	2.11 ± 0.31 ^{†,*}	1.18 ± 0.12	2.06 ± 0.32 ^{†,*}
	R	1.13 ± 0.11	1.91 ± 0.27 [†]	1.19 ± 0.13	2.19 ± 0.38 [†]	1.21 ± 0.14	2.10 ± 0.32 ^{†,*}
Occipital	L	1.10 ± 0.05	1.57 ± 0.19 ^{†,*}	1.16 ± 0.07	1.73 ± 0.25 ^{†,*}	1.16 ± 0.06	1.73 ± 0.28 ^{†,*}
	R	1.11 ± 0.06	1.60 ± 0.17 ^{†,*}	1.16 ± 0.08	1.78 ± 0.24 ^{†,*}	1.19 ± 0.08	1.76 ± 0.21 ^{†,*}
PCC		1.20 ± 0.13	2.04 ± 0.28 [†]	1.30 ± 0.16	2.43 ± 0.42 [†]	1.31 ± 0.16	2.42 ± 0.41 [†]

CTL: healthy control, eAD: early Alzheimer’s disease, DVR_r: DVR values calculated from reference tissue method using cerebellar cortex, DVR_L: DVR from dynamic [¹¹C]PiB PET data and Logan plot, SUVR: standardized uptake value ratio. [†] $p < 0.00001$ in comparing eAD and CTL subjects, * $p < 0.05$ in comparison with PCC.

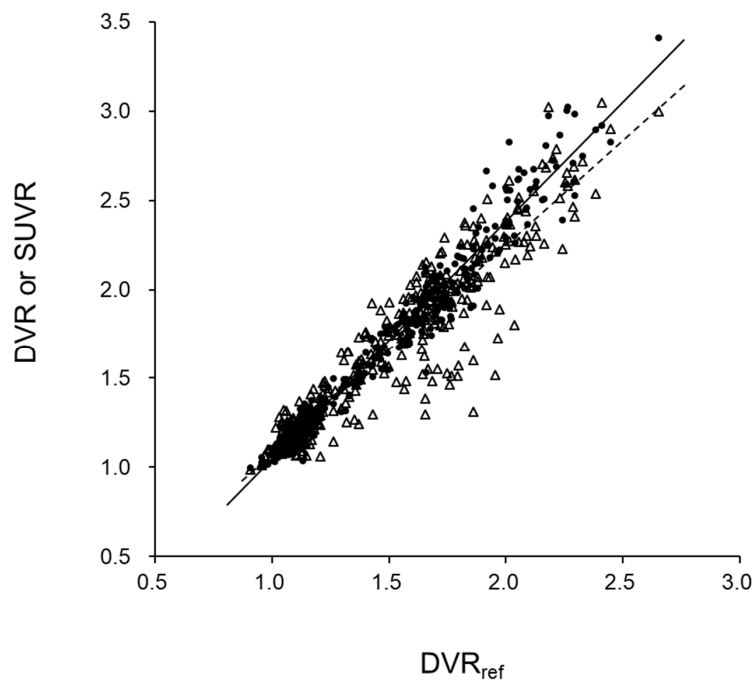


Figure 4. Regional values from all subjects were plotted to observe correlations between DVR_r vs. DVR_L (●) and DVR_r vs. SUVR (Δ). DVR_r and DVR_L showed better correlation (solid line; $y = 1.34x - 0.30$, $r^2 = 0.97$) than DVR_r and SUVR (dashed line; $y = 1.17x - 0.09$, $r^2 = 0.88$).

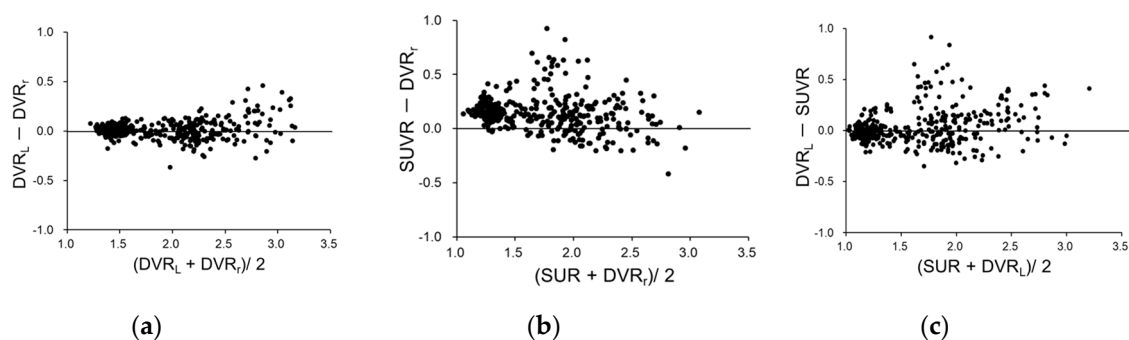


Figure 5. Balnd–Altman plots for DVR_r vs. DVR_L (a), DVR_r vs. SUVR (b), and DVR_L vs. SUVR (c) correlation. (a,b) are plots after correction with equations of linear regression.

Figure 6 shows a comparison of the metric distributions for the eAD and CTL groups. Cortical maximum values, the highest cortical mean value among all regions of frontal, temporal, parietal and occipital lobes, and those from the PCC were compared among three different methods. The PCC tended to show greater values than the cortical maximum, although they were not significantly different. According to the ROC analysis, the optimal threshold values for differentiating eAD and CTL subjects were 1.5, 1.7, and 1.6 for DVR_r , DVR_L , and SUVR, respectively. These thresholds clearly differentiated eAD from CTL for all metrics. The area under the curves (AUC) values were >0.99 for DVR_r and DVR_L , and 0.988 for SUVR in the ROC analysis.

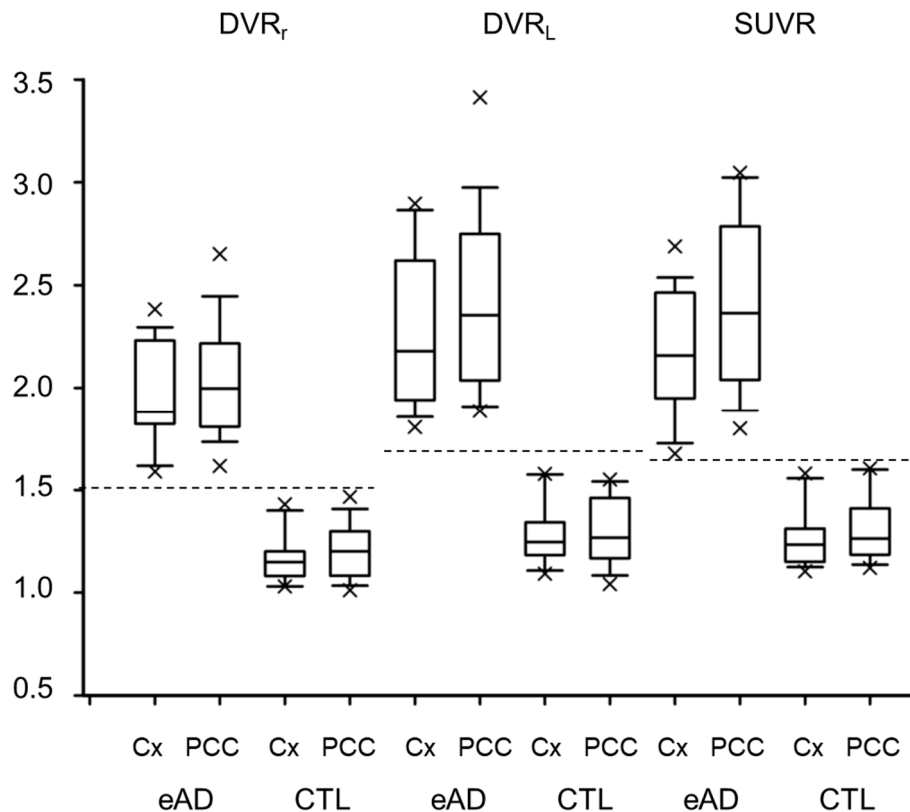


Figure 6. Cortical maximum values (Cx) of eAD and CTL obtained from each image. The posterior cingulate cortex (PCC) showed greater values than the cortical maximum among frontal, temporal, parietal, and occipital lobes. Dashed lines show optimal thresholds between eAD and CTL subjects. × is outlier of each group.

4. Discussion

The present study evaluated feasibility of our new noninvasive IDIF method for the quantitative $[^{11}\text{C}]\text{PiB}$ PET/MRI study by comparing the results with those from the reference tissue graphical method as well as SUVR. We applied a Hill-type metabolite correction for estimation of the true input function (C_p) in the IDIF, which was applied for DV image calculation in a couple of previous $[^{11}\text{C}]\text{PiB}$ studies [2,5]. All metrics were compared after normalization using the cerebellar cortical values as a reference, that is, DVR_L obtained from the DV image of the Logan plot, DVR_r calculated by the reference tissue graphical plot method, and SUVR. The correlation of regional DVR_L and DVR_r values was excellent, while SUVR showed a greater variance and a slightly inferior correlation coefficient compared with the two DVRs. Differences in metrics between the eAD and CTL groups were greater in the quantitative DVRs than in SUVR, suggesting that DVR images may provide better diagnostic performance than SUVR, although the two groups were differentiated well by the appropriate threshold for each metric determined in the present population. In the comparison of

DVR_r and DVR_L , the differences in cortical values between the two groups were greater and the image contrast was better in DVR_L than in DVR_r . Thus, if a 70 min dynamic [^{11}C]PiB PET/MRI scan is available, DVR_L image calculation with IDIF and the Hill-type correction seems to be a recommended method for quantitative analysis. However, if a patient cannot stay in the same position during a long dynamic scan, SUVR also provides reasonable results. In cases of borderline stage dementia, 70 min dynamic [^{11}C]PiB PET/MRI scans and quantitative DVR image calculation are recommended.

Recently, the impact of amyloid and tau imaging has significantly increased in terms of pathologic evidence for differential diagnosis of eAD [1]. The molecular imaging based on such findings is considered to be more reliable than diagnosis from clinical symptoms or changes in cerebral energy metabolism, which have been used in the clinical setting for a long time, although recent advanced [^{18}F]fluorodeoxy glucose (FDG)-PET studies showed similar diagnostic ability [19,20]. SUVR images in amyloid PET and their visual inspection may be sufficient for clinical diagnosis based on positive/negative discrimination according to the amyloid imaging guidelines or instructions [10]. However, for follow-up studies or multicenter studies, quantitative or semiquantitative indices are needed for comparisons of the severities and clinical stages of AD patients. In the present study, DVR_L showed the greatest difference among the three metrics between the eAD and CTL groups. Appropriate DVR calculation will provide a reliable index for longitudinal and multicenter comparisons.

Our previous studies established the IDIF method using a PET/MRI scanner for estimation of the arterial input of PET tracers [6,7,14]. However, the input functions should be corrected if the concentration of arterial blood radioactivity includes substantial metabolites of the tracer. Because several previous studies showed changes in the unmetabolized [^{11}C]PiB fraction as a function of time measured by high-performance liquid chromatography (HPLC) or thin-layer chromatography (TLC) [2,4], we were able to assume the true input curves by applying a Hill-type function estimated from the data of those previous studies. Nonlinear least squares fitting estimated appropriate constants for the function, and the unmetabolised fraction curve estimated the true input well (Figure 1). Using this function, each IDIF was corrected to the true input function (C_p), which provided an excellent Logan plot curve with good linearity in the last phase of 50–70 min after injection (Figure 2). There were no cases showing poor linearity of the plot in this phase.

We calculated DVR_r images using the Logan's reference tissue graphical method [18]. The cerebellar cortical ROIs were easier to create than the ICA ROIs for IDIF, and the stable TACs could be applied for graphical plot image calculation. Good-quality quantitative images were available, although the contrast of the gray and white matters was slightly inferior to DVR_L calculated by IDIF (Figure 3). Regional DVR_r values were slightly lower than DVR_L , which is similar to a previous result by Lopresti et al. [2]. In their study, three images calculated from arterial blood sampling with metabolite collection, IDIF, and SUVR showed similar regional values, but the reference tissue graphical method (DVR_r) showed slightly lower regional values.

We did not sample arterial blood in the present study, which may be a limitation. However, estimating the plasma input function from arterial blood sampling and metabolite correction may not be an ideal method because the plasma counts and unmetabolized fraction obtained from HPLC or TLC may include substantial errors. Mourik et al. admitted the unreliability of plasma counts which were sometimes influenced by sticking of the [^{11}C]PiB due to its high lipophilic property, and suggested that IDIFs might be more reliable [5]. The input functions obtained by arterial blood sampling and the IDIF method were not corrected for the dispersion effect of peripheral arteries in their study. The reference tissue graphical plot method is assumed to be corrected for all these possible biases of metabolites and dispersion, which could make it the most acceptable method for studies of lipophilic ligand kinetics if a reference region can be determined appropriately.

5. Conclusions

The noninvasive IDIF method for [^{11}C]PiB PET/MRI provided quantitative DV and DVR with high-quality images. The accuracy of DVR_L was almost identical to that of DVR_r , calculated by

the reference tissue graphical plot method, with excellent correlation. SUVR images also showed acceptable results as a quantitative metric despite their greater variability compared with DVR images. If a long dynamic PET/MRI scan is available, quantitative DVR images calculated using the IDIF or a reference tissue TAC are recommended for patient follow-ups or multicenter studies.

Author Contributions: Conceptualization, H.O.; methodology, M.I. and H.O.; validation, H.O. and T.T.; formal analysis, M.I. and H.O.; investigation, M.I., T.T., T.M., A.M. and H.O.; resources, M.I., H.K., and H.O.; data curation, T.T. and H.O.; writing—original draft preparation, H.O.; writing—review and editing, T.T., Y.K. and H.O.; visualization, M.I. and H.O.; project administration, M.I., H.K. and H.O.; funding acquisition, H.O. All authors have read and agreed to the published version of the manuscript.

Funding: This work was partly funded by a Grant-in-Aid for Scientific Research from the Japan Society for the Promotion of Science (18H02763).

Acknowledgments: The authors thank Hiroshi Oikawa and the staff of the Biomedical Imaging Research Center and doctors in the Departments of Neurology and Psychiatry, Faculty of Medical Sciences, University of Fukui for technical and clinical support.

Conflicts of Interest: The authors declare no conflict of interest.

References

- Jack, C.R., Jr.; Bennett, D.A.; Blennow, K.; Carrillo, M.C.; Dunn, B.; Haeberlein, S.B.; Holtzman, D.M.; Jagust, W.; Jessen, F.; Karlawish, J.; et al. NIA-AA Research Framework: Toward a biological definition of Alzheimer's disease. *Alzheimers Dement.* **2018**, *14*, 535–562. [[CrossRef](#)]
- Lopresti, B.J.; Klunk, W.E.; Mathis, C.A.; Hoge, J.A.; Ziolkowski, S.K.; Lu, X.; Meltzer, C.C.; Schimmel, K.; Tsopelas, N.D.; DeKosky, S.T.; et al. Simplified quantification of Pittsburgh Compound B amyloid imaging PET studies: A comparative analysis. *J. Nucl. Med.* **2005**, *46*, 1959–1972. Available online: <http://jnm.snmjournals.org/content/46/12/1959.full.pdf+html> (accessed on 24 October 2020).
- Yaqub, M.; Tolboom, N.; Boellaard, R.; van Berckel, B.N.; van Tilburg, E.W.; Luurtsema, G.; Scheltens, P.; Lammertsma, A.A. Simplified parametric methods for [¹¹C]PIB studies. *Neuroimage* **2008**, *42*, 76–86. [[CrossRef](#)] [[PubMed](#)]
- Price, J.C.; Klunk, W.E.; Lopresti, B.J.; Lu, X.; Hoge, J.A.; Ziolkowski, S.K.; Holt, D.P.; Meltzer, C.C.; DeKosky, S.T.; Mathis, C.A. Kinetic modeling of amyloid binding in humans using PET imaging and Pittsburgh Compound-B. *J. Cereb. Blood Flow Metab.* **2005**, *25*, 1528–1547. [[CrossRef](#)] [[PubMed](#)]
- Mourik, J.E.; Lubberink, M.; Schuitmaker, A.; Tolboom, N.; van Berckel, B.N.; Lammertsma, A.A.; Boellaard, R. Image-derived input functions for PET brain studies. *Eur. J. Nucl. Med. Mol. Imaging* **2009**, *36*, 463–471. [[CrossRef](#)] [[PubMed](#)]
- Okazawa, H.; Higashino, Y.; Tsujikawa, T.; Arishima, H.; Mori, T.; Kiyono, Y.; Kimura, H.; Kikuta, K. Noninvasive method for measurement of cerebral blood flow using O-15 water PET/MRI with ASL correlation. *Eur. J. Radiol.* **2018**, *105*, 102–109. [[CrossRef](#)] [[PubMed](#)]
- Okazawa, H.; Tsujikawa, T.; Higashino, Y.; Kikuta, K.; Mori, T.; Makino, A.; Kiyono, Y. No significant difference found in PET/MRI CBF values reconstructed with CT-atlas-based and ZTE MR attenuation correction. *Eur. J. Nucl. Med. Mol. Imaging Res.* **2019**, *9*, 26. [[CrossRef](#)]
- Gunn, R.N.; Sargent, P.A.; Bench, C.J.; Rabiner, E.A.; Osman, S.; Pike, V.W.; Hume, S.P.; Grasby, P.M.; Lammertsma, A.A. Tracer kinetic modeling of the 5-HT_{1A} receptor ligand [carbonyl-¹¹C]WAY-100635 for PET. *Neuroimage* **1998**, *8*, 426–440. [[CrossRef](#)] [[PubMed](#)]
- Hosokawa, C.; Ishii, K.; Kimura, Y.; Hyodo, T.; Hosono, M.; Sakaguchi, K.; Usami, K.; Shimamoto, K.; Yamazoe, Y.; Murakami, T. Performance of ¹¹C-Pittsburgh Compound B PET Binding Potential Images in the Detection of Amyloid Deposits on Equivocal Static Images. *J. Nucl. Med.* **2015**, *56*, 1910–1915. [[PubMed](#)]
- Yamane, T.; Ishii, K.; Sakata, M.; Ikari, Y.; Nishio, T.; Ishii, K.; Kato, T.; Ito, K.; Senda, M.; J-ADNI Study Group. Inter-rater variability of visual interpretation and comparison with quantitative evaluation of ¹¹C-PiB PET amyloid images of the Japanese Alzheimer's Disease Neuroimaging Initiative (J-ADNI) multicenter study. *Eur. J. Nucl. Med. Mol. Imaging* **2017**, *44*, 850–857. [[PubMed](#)]
- Levin, C.S.; Maramraju, S.H.; Khalighi, M.M.; Deller, T.W.; Delso, G.; Jansen, F. Design features and mutual compatibility studies of the time-of-flight PET capable GE SIGNA PET/MR system. *IEEE Trans. Med. Imaging* **2016**, *35*, 1907–1914. [[CrossRef](#)] [[PubMed](#)]

12. Wiesinger, F.; Sacolick, L.I.; Menini, A.; Kaushik, S.S.; Ahn, S.; Veit-Haibach, P.; Delso, G.; Shanbhag, D.D. Zero TE MR bone imaging in the head. *Magn. Reson. Med.* **2016**, *75*, 107–114. [[CrossRef](#)] [[PubMed](#)]
13. Delso, G.; Kemp, B.; Kaushik, S.; Wiesinger, F.; Sekine, T. Improving PET/MR brain quantitation with template-enhanced ZTE. *Neuroimage* **2018**, *181*, 403–413. [[CrossRef](#)] [[PubMed](#)]
14. Okazawa, H.; Ikawa, M.; Jung, M.; Maruyama, R.; Tsujikawa, T.; Mori, T.; Rahman, M.G.M.; Makino, A.; Kiyono, Y.; Kosaka, H. Multimodal analysis using [¹¹C]PiB-PET/MRI for functional evaluation of patients with Alzheimer’s disease. *EJNMMI Res.* **2020**, *10*, 30. [[CrossRef](#)] [[PubMed](#)]
15. Islam, M.M.; Tsujikawa, T.; Mori, T.; Kiyono, Y.; Okazawa, H. Estimation of arterial input by a noninvasive image derived method in brain H₂¹⁵O PET study: Confirmation of arterial location using MR angiography. *Phys. Med. Biol.* **2017**, *62*, 4514–4524. [[CrossRef](#)] [[PubMed](#)]
16. Logan, J.; Fowler, J.S.; Volkow, N.D.; Wolf, A.P.; Dewey, S.L.; Schlyer, D.J.; MacGregor, R.R.; Hitzemann, R.; Bendriem, B.; Gatley, S.J.; et al. Graphical analysis of reversible radioligand binding from time-activity measurements applied to [N-¹¹C-methyl]-(-)-cocaine PET studies in human subjects. *J. Cereb. Blood Flow Metab.* **1990**, *10*, 740–747. [[CrossRef](#)] [[PubMed](#)]
17. Okazawa, H.; Yamauchi, H.; Sugimoto, K.; Magata, Y.; Kudo, T.; Yonekura, Y. Effects of metabolite correction for arterial input function on quantitative receptor images with ¹¹C-flumazenil in clinical PET studies. *J. Comput. Assist. Tomogr.* **2004**, *28*, 428–435. [[CrossRef](#)] [[PubMed](#)]
18. Logan, J.; Fowler, J.S.; Volkow, N.D.; Wang, G.J.; Ding, Y.S.; Alexoff, D.L. Distribution volume ratios without blood sampling from graphical analysis of PET data. *J. Cereb. Blood Flow Metab.* **1996**, *16*, 834–840. [[CrossRef](#)] [[PubMed](#)]
19. Pagani, M.; Giuliani, A.; Öberg, J.; Chincarini, A.; Morbelli, S.; Brugnolo, A.; Arnaldi, D.; Picco, A.; Bauckneht, M.; Buschiazzo, A.; et al. Predicting the transition from normal aging to Alzheimer’s disease: A statistical mechanistic evaluation of FDG-PET data. *Neuroimage* **2016**, *141*, 282–290. [[CrossRef](#)] [[PubMed](#)]
20. Brugnolo, A.; De Carli, F.; Pagani, M.; Morbelli, S.; Jonsson, C.; Chincarini, A.; Frisoni, G.B.; Galluzzi, S.; Perneczky, R.; Drzezga, A.; et al. Head-to-head comparison among semi-quantification tools of brain FDG-PET to aid the diagnosis of prodromal Alzheimer’s disease. *J. Alzheimers Dis.* **2019**, *68*, 383–394. [[CrossRef](#)]

Publisher’s Note: MDPI stays neutral with regard to jurisdictional claims in published maps and institutional affiliations.



© 2020 by the authors. Licensee MDPI, Basel, Switzerland. This article is an open access article distributed under the terms and conditions of the Creative Commons Attribution (CC BY) license (<http://creativecommons.org/licenses/by/4.0/>).